*Center for Turbulence Research*
*Annual Research Briefs 2014*

# Taming nonlinear instability for discontinuous Galerkin scheme with artificial viscosity

By **Y. Lv** and **M. Ihme**

## 1. Motivation and objectives

Over recent years, the advantages of discontinuous Galerkin (DG) scheme has been demonstrated in applications to smooth problems. For conservation laws, the interaction among different physical invariants can lead to discontinuous solutions. In those cases, strong numerical oscillations are triggered in the numerical solution through the DG discretization. To address the issue that arises due to nonlinearities of the problem, certain stabilization mechanisms must be imposed. Popular examples include limiting techniques and artificial viscosity (AV). Over the past few years, several limiters have been proposed, for example, Cockburn & Shu (1998), Qiu & Shu (2005), and Krivodonova (2007). The main idea of suppressing oscillation is to modify the local solution by considering the information about solutions in neighboring cells. The main shortcomings of limiting are (i) poor adaptability to elements with complex shapes; (ii) accuracy reduction in regions of smooth solutions; and (iii) lack of support to the order higher than DGP2 (quadratic polynomial representation).

Realization of these shortcomings has made the design artificial viscosity method for DG a central focus of recent research activities. Hartmann (2006) used an AV formula based on a scaled residual for steady-state problems. Persson & Peraire (2006) proposed a non-smoothness sensor for estimating artificial viscosity. The sensor uses information of higher-order moments and results in a viscosity quantity scaled with $h/p$, where $h$ is the element size and $p$ is the order of the polynomial. The success of this formulation has been demonstrated in implicit RANS simulations by Nguyen *et al.* (2007). Because of numerical issues associated with piecewise constant artificial viscosity, Barter & Darmofal (2010) suggested imposing viscosity continuity across adjacent elements using a PDE-based approach. Another modification was recently proposed by Casoni *et al.* (2013). In contrast to the $h/p$-scaling, they used an artificial viscosity that scales with $h^p$, and demonstrated improved performance on coarse grids up to DGP11 in a 1D setting. As artificial viscosity methods have become more popular, other interesting formulations have also appeared in the literatures. For example, Yu & Yan (2013) implemented a viscosity formulation for DG scheme, which originated from the finite-difference community (Kawai & Lele 2008). With this formulation, fine scales in Rayleigh-Taylor instability were successfully captured with orders up to DGP3. Zingan *et al.* (2013) implemented the entropy-viscosity formulation for DG scheme, which was initially proposed by Guermond & Pasquetti (2008) for finite volume methods. This idea leads to the estimation of artificial viscosity based on the local residual of the entropy equation of the nonlinear conservation system.

In the present study, we propose a new AV-approach for the DG scheme, specifically tailored for explicit time stepping. Technically this scheme consists of the following steps: (i) re-examine the AV formulation of Persson & Peraire (2006); (ii) identify and amend the shortcomings of this method by conducting stability analysis and developing a new detector; and (iii) demonstrate the performance through numerical tests.

## 2. Methodology

### 2.1. *Governing equations*

We consider the solution of the conservation equations in the most general form

$$\partial_t \boldsymbol{U} + \nabla \cdot \boldsymbol{F} = 0 \ , \tag{2.1}$$

which might contain discontinuities in the solution. To stabilize the solution procedure, we introduce a linear Laplacian regularization on the right side,

$$\partial_t \boldsymbol{U} + \nabla \cdot \boldsymbol{F} = \nabla \cdot (\widehat{\mu}_e \nabla \boldsymbol{U}) \ , \tag{2.2}$$

in which $\widehat{\mu}_e$ quantifies the amount of artificial viscosity that is added locally for suppressing nonlinear instabilities.

### 2.2. *Discretization and AV formulation*

The DG discretization follows the standard conventions and readers are referred to our previous work (Lv & Ihme 2013*a*,*b*, 2014) for more details. In a DG cell $\Omega_e$, the solution is approximated as

$$\boldsymbol{U}_h^e(t,\boldsymbol{x}) = \sum_{l=1}^{N_p} \widetilde{\boldsymbol{U}}_l^e(t)\boldsymbol{\phi}_l^e(\boldsymbol{x}) \ , \tag{2.3}$$

where $N_p$ is the number of bases. In the present study, an orthogonal basis is used, $N_p = (p+1)(p+2)/2$, where $p$ is the order of the polynomial representation. In the following derivation, we assume that the basis indices are ordered with increasing polynomial order. A Rusanov flux (Rusanov 1961) is used as a Riemann solver, and the BR2 scheme (Bassi & Repay 2000) is used for discretization of the diffusion operator.

Here we briefly summarize the AV formulation of Persson & Peraire (2006). This formulation is based on a non-smoothness indicator and a mapping function to evaluate the element-wise viscosity. The non-smoothness indicator is defined as follows:

$$S_e = \frac{\left(\boldsymbol{U}_h^e - \widehat{\boldsymbol{U}}_h^e, \boldsymbol{U}_h^e - \widehat{\boldsymbol{U}}_h^e\right)_e}{(\boldsymbol{U}_h^e, \boldsymbol{U}_h^e)_e}, \tag{2.4}$$

in which $\widehat{\boldsymbol{U}}_h^e$ represents the truncated solution up to order $p-1$, and is written as

$$\widehat{\boldsymbol{U}}_h^e(\boldsymbol{x},t) = \sum_{l=1}^{N_p-(p+1)} \widetilde{\boldsymbol{U}}_l^e(t)\boldsymbol{\phi}_l^e(\boldsymbol{x}) \ . \tag{2.5}$$

After evaluating $S_e$, the following mapping is applied to determine the amount of artificial viscosity required for the target element,

$$\widehat{\mu}_e = \begin{cases} 0, & \text{if } S_e < S_0 - \kappa \\ \frac{\mu_0}{2}\left(1 + \sin\frac{\pi(S_e - S_0)}{2\kappa}\right), & \text{if } S_0 - \kappa \le S_e \le S_0 + \kappa \\ \mu_0, & \text{if } S_e > S_0 + \kappa, \end{cases} \tag{2.6}$$

where several parameters have been introduced. These parameters can be estimated using the arguments $S_0 \sim \log(1/p^4)$, $\mu_0 \sim h/p$, and $\kappa$ is an empirical parameter that is sufficiently large. This AV formula was originally proposed for an implicit simulation. Based on numerical tests, we found that the original version of this formula has shortcomings for application to explicit time integration. More specifically, there are two problems that need to be addressed: (1) difficulty in determining $\mu_0$. Although a scaling argument is given, a rigorous guideline to determining $\mu_0$ is required. Otherwise, either the discontinuity will be excessively smeared out, or not enough diffusion will be added to suppress the oscillations. In addition, the large value of $\mu_0$ can lead to substantial numerical stiffness of the discretized system. If $\mu_0$ is naively set to $h/p$, for most cases, the time-step size has to be significantly reduced to guarantee stability. For implicit aerodynamic computations, $\mu_0$ can be fine-tuned around steady-state solutions to produce optimal shock profiles. But for unsteady simulations, having a solid approach for evaluating $\mu_0$ and using it during the entire simulation is desirable. A guideline for determining $\mu_0$ will be proposed based on the eigenmode argument and stability analysis; (2) difficulty in determining $\kappa$. In Eq. (2.6), the role of $\kappa$ is to control the selectivity; in other words, $\kappa$ determines candidate elements to which artificial dissipation should be added. However, it is difficult to apply because there is no physical interpretation associated with $\kappa$. If $\kappa$ is too small, the artificial diffusion tends to be added on smooth solutions. To overcome this drawback, a novel algorithm is required to account for the selectivity of trouble cells and $\kappa$ is fixed to $10S_0$.

### 2.3. *Improvement 1: the AV magnitude for explicit time stepping*

In order to facilitate explicit time stepping, we require that the amount of artificial viscosity is not so large that it significantly influences the time-step size that should be determined by convection. The rationale for this argument is that the nature of the hyperbolic equation determines the problem to be dominated by convective modes. The artificial viscosity is purposely added to suppress the nonlinear interaction between different modes (or nonlinear instability). Otherwise, both the accuracy and consistency are questionable. Based on this argument, we are able to find $\mu_0$ in Eq. (2.6) from the following analysis.

We characterize the convection mode in the discretized system using the smallest eigenvalue along the real axis, $\Re(\lambda^{adv})_{\min}$ $(< 0)$. The addition of AV transforms the eigenvalue structure and leads to the change of $\Re(\lambda^{adv})_{\min}$ to $\Re(\lambda^{adv+AV})_{\min}$, which can be approximated as

$$\Re(\lambda^{adv+AV})_{\min} \approx \Re(\lambda^{adv})_{\min} + \Re(\lambda^{AV})_{\min} = \beta \Re(\lambda^{adv})_{\min} \ , \tag{2.7}$$

in which $\beta$ is the key parameter determining both the amount of AV and the time-step size of the explicit DG-scheme. Based on the above argument, a suitable choice for $\beta$ is $1 < \beta < 2$. If $\beta \geq 2$, the diffusion exceeds convection and locally dominates the flow field. Therefore, the range of the parameter, $\beta$, that is introduced here is significantly constrained. From numerical experiments, we found a rather robust selection of $\beta$, which is $\beta = 1.15$ for linear cases and $\beta = 1.5$ for nonlinear cases. In order to utilize this scaling argument for finding $\mu_0$, we conducted a stability analysis in which AV is added locally into one element on a 1D domain. Based on this analysis, the following estimations can be obtained:

$$\Re(\lambda^{adv})_{\min} \approx -C_1(p)\frac{a}{h} \ , \tag{2.8}$$

$$\Re(\lambda^{AV})_{\min} \approx -C_2(p)\frac{\mu_0}{h^2} \ , \tag{2.9}$$

in which $a$ denotes the maximum characteristic speed over the computational domain; and $h$ is the element size; the constants $C_1$ and $C_2$ are both functions of $p$ and can be determined numerically, as shown in Figure 1 and in Table 1. Combining these relations

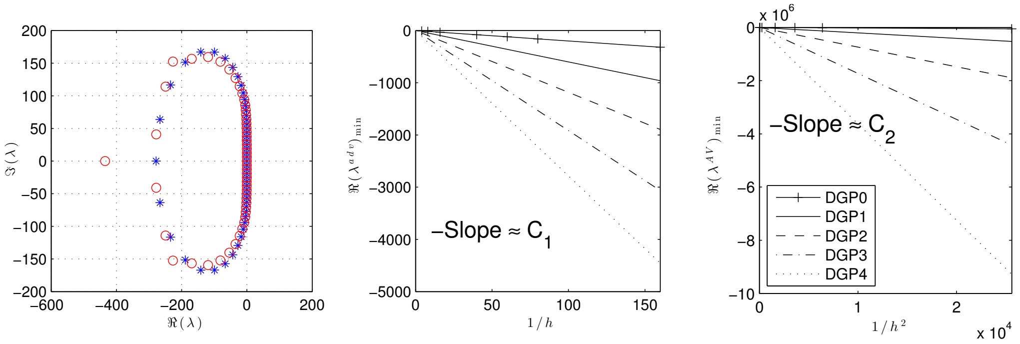

(a) Reformed eigen-structure by AV

(b) Scaling of $\Re(\lambda^{adv})_{\min}$

(c) Scaling of $\Re(\lambda^{AV})_{\min}$

FIGURE 1. Eigen-structure reformation by AV and the scaling of $\Re(\lambda^{adv})_{\min}$ and $\Re(\lambda^{AV})_{\min}$ with respect to element size $h$ ((a) $*$ pure advection $\circ$ advection with AV ).

| Order | $C_1$ | $C_2$ |
|---|---|---|
| DGP0 | 2.0 | 2.0 |
| DGP1 | 6.0 | 20.5 |
| DGP2 | 11.8 | 74.0 |
| DGP3 | 19.1 | 173.0 |
| DGP4 | 27.8 | 362.3 |

TABLE 1. Constants derived from the stability analysis for different orders of polynomial bases.

with Eq. (2.7) yields the following expression,

$$\mu_0 = (\beta - 1)\frac{C_1(p)}{C_2(p)} a h \, . \tag{2.10}$$

$a/h$ can be expressed as time step under the well-known RKDG CFL constraint (Cockburn & Shu 2001),

$$\frac{a\Delta t}{h} \leq \frac{1}{\beta(2p+1)} \, , \tag{2.11}$$

where $\beta$ is added to account for the eigenvalue amplification by AV. With this, we can relate $\mu_0$ to the time-step size,

$$\mu_0 = \frac{\beta - 1}{\beta(2p+1)} \frac{C_1(p)}{C_2(p)} \frac{h^2}{\Delta t} \, . \tag{2.12}$$

Since $\Delta t \sim \mathcal{O}(h)$ for the convection-dominated problem, the scaling of $\mu_0$, $\mu_0 \sim \mathcal{O}(h)$ is consistent with that proposed by Persson and Peraire. However, the advantage of this new formulation is that a rigorous expression is given for different orders of bases, instead of a simple scaling argument. Moreover, this new formulation balances the AV performance (see Section 3 for details) and time-stepping efficiency for explicit DG schemes.

### 2.4. *Improvement 2: trouble-cell selectivity*

Instead of using $\kappa$ for trouble-cell selectivity, we propose the following detection procedure, which is based on monitoring the entropy variation in each DG-cell. The idea is illustrated in Figure 2. Let us suppose we are able to record the maximum and minimum

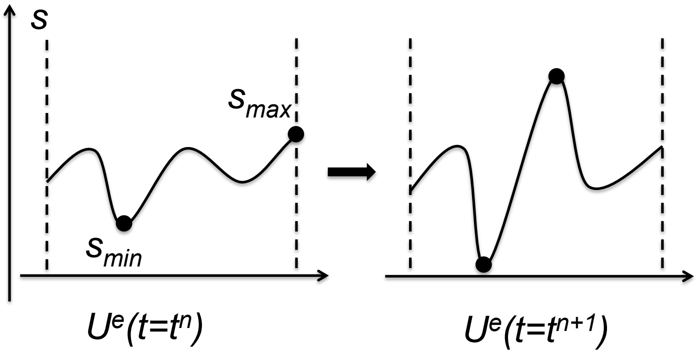

FIGURE 2. (Color online) Illustration of an entropy-based instability detector.

entropy of the solution $\boldsymbol{U}_h^e$ in a DG cell at $t = t^n$. After one time step, the entropy profile of this cell will vary. If we find that the entropy overshot and undershot in the interior part of the cell, it is likely that the cell is troubled by nonlinear instability. Now the issue is how to implement this physical observation in DG-cells. To numerically search the entropy minimum and maximum in $\Omega_e$ can be very costly and might fail. Therefore, we have to implement this idea in a discrete setting as an approximation to its continuous counterpart. For this, we first define the set of quadrature points that are used to evaluate the integral in the governing equation to be $\mathcal{D}$. $\mathcal{D}$ includes quadrature points on $\Omega_e \cup \partial\Omega_e^-$, in which superscript '$-$' denotes the exterior. Let us define another set of quadrature point $\mathcal{D}_{chk}$, which only includes the quadrature points on the interior part of $\Omega_e$, $\Omega_e \setminus \partial\Omega_e^+$. The detecting procedure is given as follows:

First, estimate the minimum and maximum of a set of entropy values that are evaluated on $\mathcal{D}$ at $t = t^n$ using

$$s_{\min} \approx \widetilde{s}_{\min} = \min_{x\in\mathcal{D}} s(U(x)) + C_3 s_{\text{ref}} \frac{h}{p+1} \ , \tag{2.13}$$

$$s_{\max} \approx \widetilde{s}_{\max} = \max_{x\in\mathcal{D}} s(U(x)) + C_4 s_{\text{ref}} \frac{h}{p+1} \ , \tag{2.14}$$

in which $s_{\text{ref}}$ accounts for the normalization, and $C_3$ and $C_4$ are constant parameters (set to 0.1).

Second, after the time advances from $t^n$ to $t^{n+1}$, check the entropy values for the set of points in $\mathcal{D}_{chk}$ and determine if $\Omega_e$ is a troubled cell using the metric:

$$\text{if } \exists x \in \mathcal{D}_{chk},\ s(U(x)) > s_{\max} \ || \ s(U(x)) < s_{min}, \text{then } \Omega_e \text{ is a troubled cell.} \tag{2.15}$$

In the case where $\Omega_e$ is a trouble cell, $\mu_0$ will be evaluated thought the approach presented in Section 2.3 and $\widehat{\mu}_e$ will be determined though Eq. (2.6), and added to the discretization.

Finally, repeat the first step for the present time level $t^{n+1}$.

## 3. Numerical tests

For the following tests, the standard Runge-Kutta time-stepping scheme is used.

### 3.1. *Burgers' equation*

For the first case, we consider the nonlinear scalar equation, also known as Burgers' equation, with $\boldsymbol{F} = \boldsymbol{U}^2/2$. The initial condition is given as

$$\boldsymbol{U}(x, 0) = 1 + \sin(2\pi x) \ , \tag{3.1}$$

on a one-dimensional periodical domain $x \in [0.0, 1.0)$. The experiment stops at $t = 1.0$ when the discontinuity is located at the center of the domain. Solution snapshots are given in Figure 3, confirming the effectiveness of the trouble-cell sensor. It can be seen that the detected trouble cells alway follow the discontinuity, so that shock-capturing errors can be localized. The simulation result without AV is also given in Figure 3(d) for comparison. It can been seen that big oscillations are triggered in the vicinity of the discontinuity, which directly leads to the blow-up right after $t = 0.3$. Results from refinement are shown in Figure 4. It can be seen that the resolution of the discontinuity is improved with $p$- or $h$-refinements.

### 3.2. *Euler equation*

In this section, we test our AV formulation by considering that Euler equations,

$$\boldsymbol{U} = (\rho,\ \rho u,\ \rho E)^T \ , \tag{3.2}$$

$$\boldsymbol{F} = (\rho u,\ \rho u \otimes u + \boldsymbol{I}p, u(\rho E + p))^T \ , \tag{3.3}$$

in which $\rho$, $u$, $p$ and $E$ refer to density, velocity, pressure, and total energy. The closure for this conservation law is the ideal gas assumption:

$$p = (\gamma - 1)\left(\rho E - \frac{\rho |u|^2}{2}\right) \ , \tag{3.4}$$

and $\gamma$, the ratio of heat capacities, is set to 1.4.

#### 3.2.1. *Sod shock tube*

The initial conditions are defined as

$$(\rho, u, p)^T = \begin{cases} (1.0,\ 0.0,\ 1.0)^T & \text{for } x \le 0.5 \ , \\ (0.125,\ 0.0,\ 0.1)^T & \text{for } x > 0.5 \ , \end{cases} \tag{3.5}$$

on a 1D domain $x \in [0.0, 1.0]$. The convergence study is conducted on this problem, and the simulation runs until $t = 0.25$. The performance of the detector is assessed in Figure 5. As we can see, the detector precisely flagged the trouble cells in the vicinity of the shock, with which the shock-capturing error can be highly localized, as shown in Figure 5(d). For the local error assessment, the exact solution is obtained with an exact refinement and the error is evaluated point-wise in $L_1$-norm. A refinement study is also conducted and the results are summarized in Figure 6. The observation is similar to that of the above test case.

#### 3.2.2. *Double Mach reflection*

This test case studies a moving shock that reflects at a wall. The setting is consistent with that described by Woodward & Colella (1984). We consider a two-dimensional domain $x^{(1)} \times x^{(2)} \in [0.0,\ 4.0] \times [0.0,\ 1.0]$. A Mach 10 shock is initially aligned with a $60^o$ angle with respect to the horizontal axis. The pre- and post-shock states take the

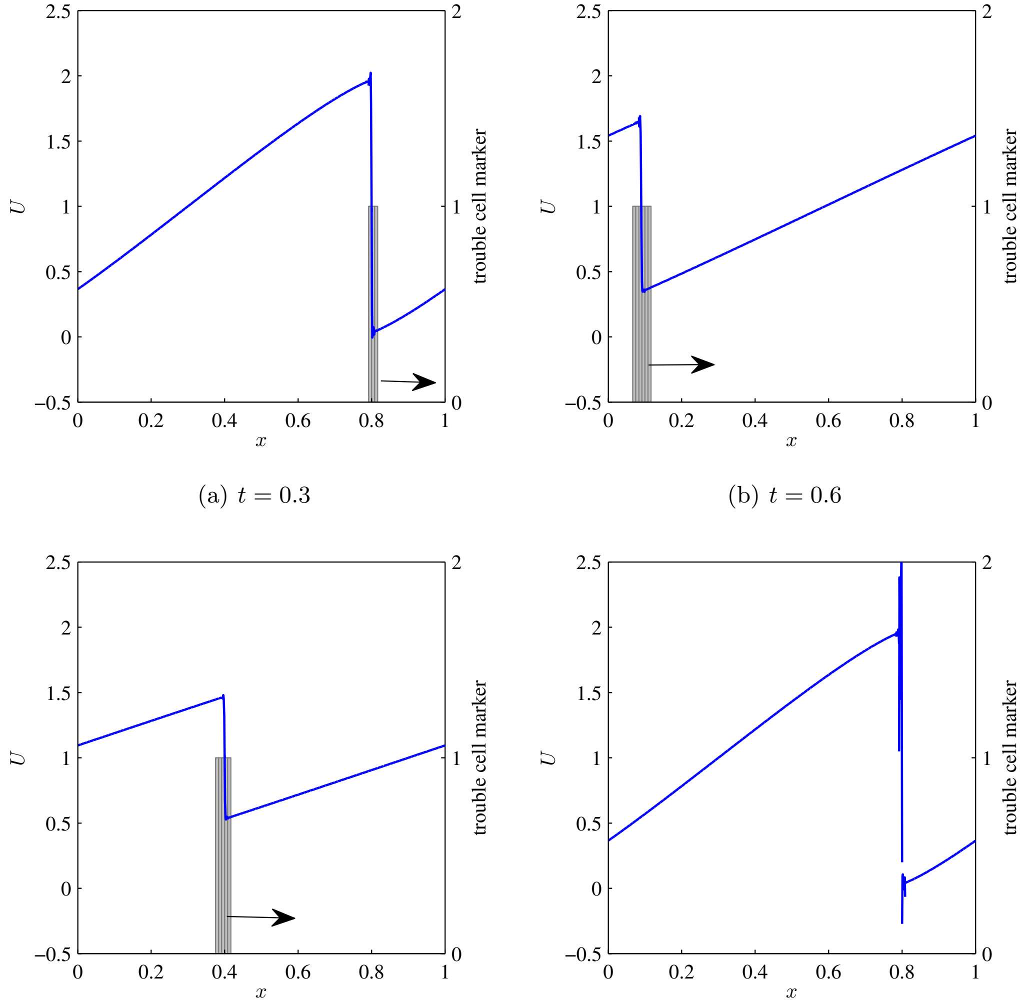

(a) $t = 0.3$ (b) $t = 0.6$

(c) $t = 0.9$ (d) $t = 0.3$ without AV

FIGURE 3. Numerical test on the trouble cell sensing for Burger's equation (DGP4 with 120 elements).

following forms

$$\boldsymbol{U}_{pre} = (1.4,\ 0.0,\ 0.0,\ 2.5)^T\ , \tag{3.6}$$

$$\boldsymbol{U}_{post} = (8.0,\ 57.16,\ 33.0\ , 563.50)^T\ , \tag{3.7}$$

and the initial condition can be prescribed as

$$\boldsymbol{U}(x, 0) = \begin{cases} \boldsymbol{U}_{pre} & x^{(1)} < \frac{1}{6} + \frac{x^{(2)}}{\sqrt{3}}\ , \\ \boldsymbol{U}_{post} & x^{(1)} \geq \frac{1}{6} + \frac{x^{(2)}}{\sqrt{3}}\ . \end{cases} \tag{3.8}$$

In order to enforce the shock-wall interaction, the left boundary and the [0.0, 1/6) part of the bottom boundary are prescribed by a supersonic inflow with the state given

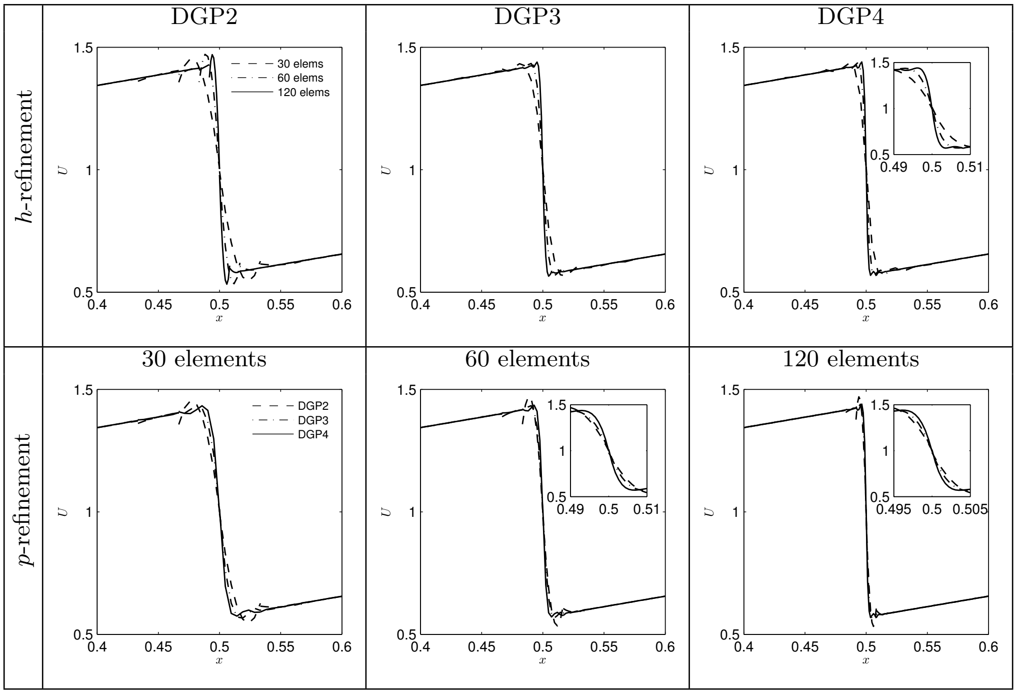

FIGURE 4. Numerical test for $h$- and $p$- refinements for Burgers' equation.

by $\boldsymbol{U}_{post}$, while the region [1/6, 4.0] of the bottom boundary is prescribed using slip wall conditions. The right boundary is prescribed by a supersonic outflow, where the Neumann condition can be safely used. Furthermore, the top boundary is a free boundary imposed analytically to describe the moving discontinuity as a function of time. At the top boundary, the jump is a function of time $x_s^{(1)} = \frac{1}{6} + \frac{1+20t}{\sqrt{3}}$. The simulation stops at t = 2.5. The refinement studies are summarized in Figure 7. The important feature of the flow field is the formulation of a wall jet along the slip line, which is very sensitive to the numerical dissipation. With $h$-refinement, we can clearly observe finer vortex structures induced by the Kelvin-Helmholtz instability. In the results generated by DGP4, a faster growth of the wall jet is observed compared to the results for DGP2, by which the jet front merges earlier with part of the Mach stem. This feature was not captured by most of the previous case studies on such a coarse mesh.

### 3.2.3. *Forward facing step*

This test case studies a Mach 3 flow passing through a wind tunnel, $[0,\ 3] \times [0,\ 1]$. A step of 0.2 unit is located at 0.6 units away from the left boundary. The left boundary is a supersonic inflow with the conditions $(\rho,\ u^{(1)},\ u^{(2)}\ p)^T = (1.4,\ 3.0,\ 0.0,\ 1.0)^T$, and the right boundary is specified by the Neumann conditions. The top and bottom boundaries are prescribed by slip walls. At the beginning, the computational domain is initialized uniformly with the inflow condition, which can be expressed in terms of solution variables:

$$\boldsymbol{U}(x,0) = (1.4,\ 4.2,\ 0.0,\ 8.8)^T\ . \tag{3.9}$$

The flow evolves until $t = 4.0$. The numerical study for this case with high-order polynomial bases is still quite rare. In order to demonstrate the potential of our method, we

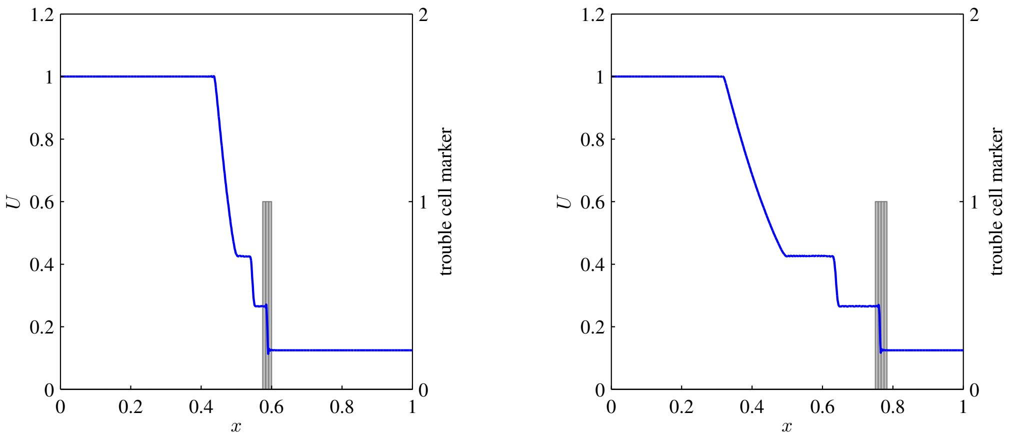

(a) density profile $t = 0.05$

(b) density profile $t = 0.15$

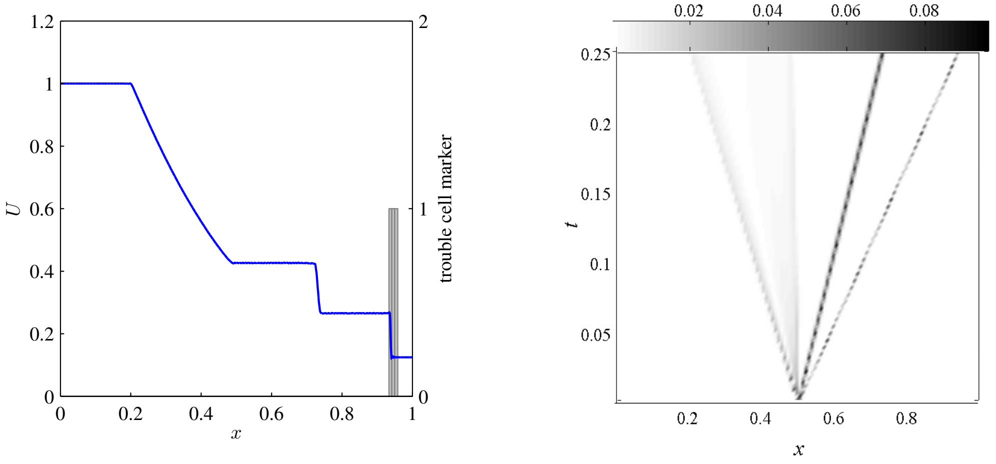

(c) density profile $t = 0.25$

(d) Local error of density in space-time

FIGURE 5. Numerical test on the sensor performance and the error locality for the 1D shock tube case (DGP4, 120 elements).

conducted the test with DGP2 (third-order) and DGP4 (fifth-order). Mesh refinement is also considered and two Cartesian meshes with $h = 0.02$ and $h = 0.01$ are used for this test. The simulation results are illustrated in Figure 8. We can clearly see the improvement by $p$- or $h$- refinement in terms of the sharpness of the wave fronts and the resolution of the top slip line from which Kelvin-Helmholtz instability is triggered. On the fine mesh, the simulation results with different bases become very close to each other. However, if we focus on the vortex structures that are resolved at the slip line, DGP4 gives finer structures than DGP2 due to the reduced numerical dissipation.

### 3.2.4. *Kelvin-Helmholtz instability*

The above two classic test cases are both shock-dominated flows, and it has been shown that under certain conditions hydrodynamic instabilities can be triggered. In this case, we would like to isolate the instability and assess the capability of high-order

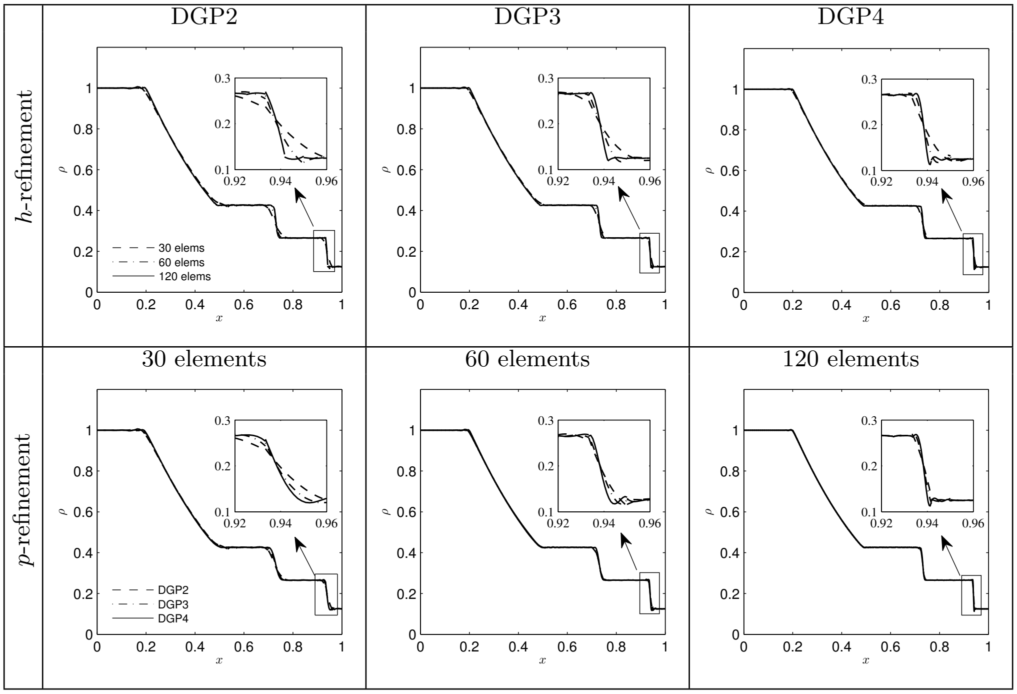

FIGURE 6. Numerical test on the refinement consistency for the 1D shock tube case.

DG schemes in resolving small scales. Hence, a classic two-dimensional simulation of the Kelven-Helmholtz instability is considered. The computational domain is a periodic square, $[-0.5,\ 0.5]^2$. The initial condition is specified as

$$\left(\rho,\ u^{(1)},\ u^{(2)},\ p\right)^T = \begin{cases} (1.0,\ 0.5+0.01\sin(2\pi x),\ 0.01\sin(2\pi x),\ 2.5)^T & \text{for } |x| \geq 0.25\ , \\ (2.0,\ -0.5+0.01\sin(2\pi x),\ 0.01\sin(2\pi x),\ 2.5)^T & \text{for } |x| < 0.25\ , \end{cases} \tag{3.10}$$

in which a single moded sin-wave is superimposed on the shear flow as a small initial perturbation. The test is conducted with the polynomial bases of different orders but the same degree of freedom for fair comparison. For DGP1, DGP2, DGP3, and DGP4, the element sizes are $h = 1/300,\ 1/200,\ 1/150$, and $1/120$, respectively. The CFL numbers are set according to Eq. (2.11), and the resultant time-step sizes are almost the same for different cases. The simulation runs to $t = 5$. Due to singularities and nonlinearities of Euler equations, there are no exact solutions for this case. Therefore, the benefits of using high-order bases continue to be in resolving smaller scale vortices and in preserving the sharp density interface, which is illustrated in Figure 9(a) and (b). The reduced numerical dissipation of the high-order scheme is also more capable of retaining the small initial perturbation and hence earlier growth of the kinetic energy. This numerical characteristics is shown in Figure 9(c).

## 4. Conclusion and outlook

In the present study, we extended the AV formulation by Persson & Peraire (2006) and propose a new AV formulation for DG, suitable specifically from explicit time integration. The proposed AV formulation is built on stability analysis for determining

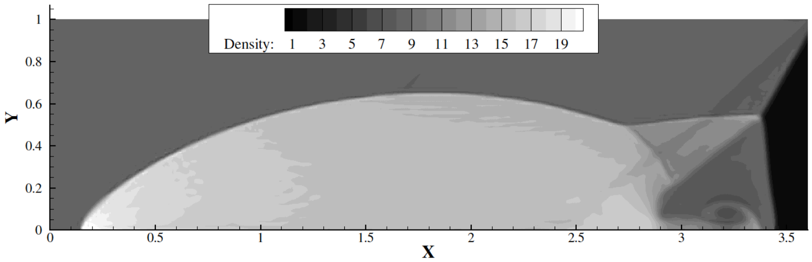

(a) DGP2, $h = 0.02$

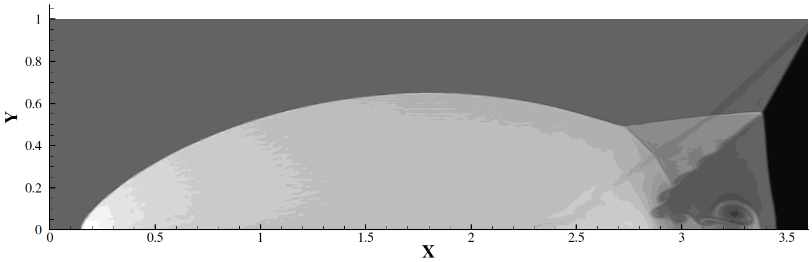

(b) DGP2, $h = 0.01$

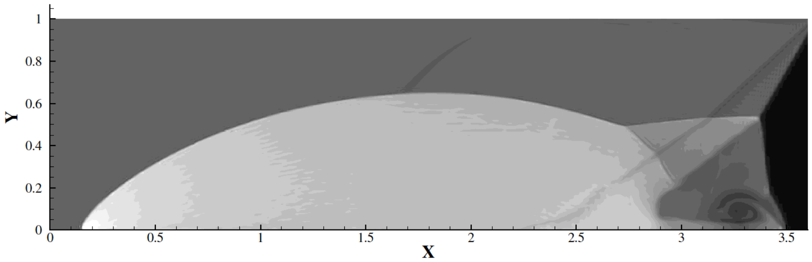

(c) DGP4, $h = 0.02$

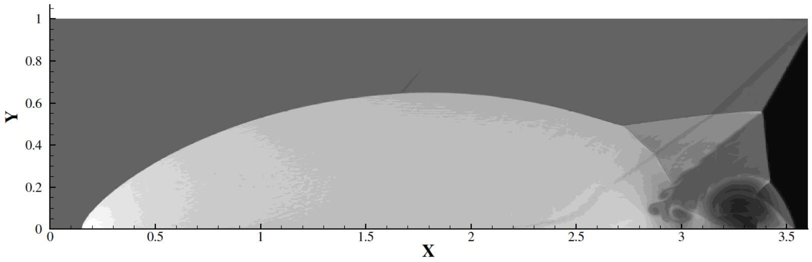

(d) DGP4, $h = 0.01$

FIGURE 7. Simulation results of the double-Mach-reflection case with different polynomial orders and mesh sizes.

the viscosity magnitude and the development of a detecting procedure for identifying trouble cells. The performance of this AV formulation was examined in the context of shock-dominated flows and was shown to be capable of supporting the order up to DGP4 (the highest we considered in this study). Artificial viscosity is activated only in the vicin-

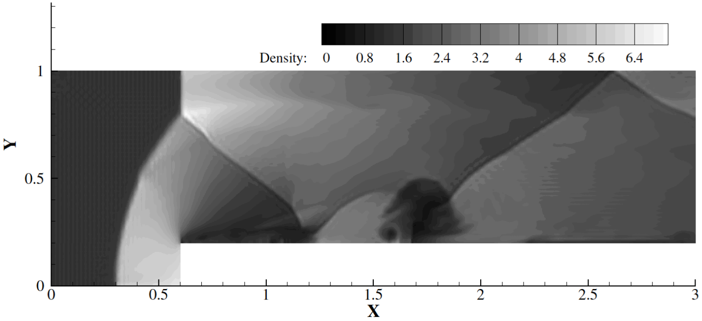

(a) DGP2, $h = 0.02$

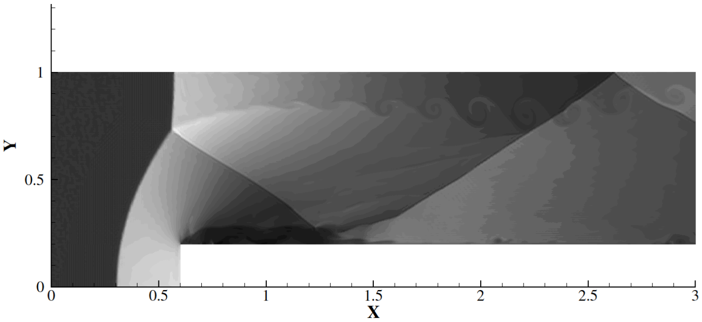

(b) DGP2, $h = 0.01$

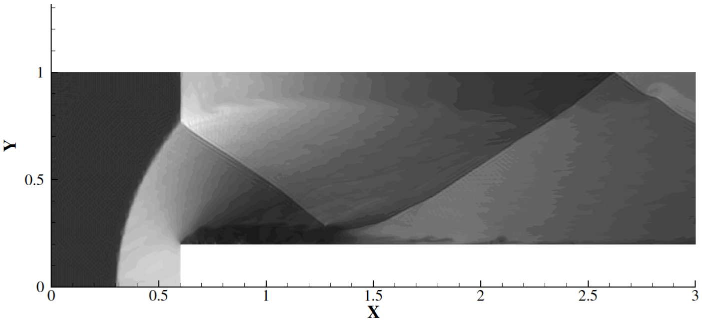

(c) DGP4, $h = 0.02$

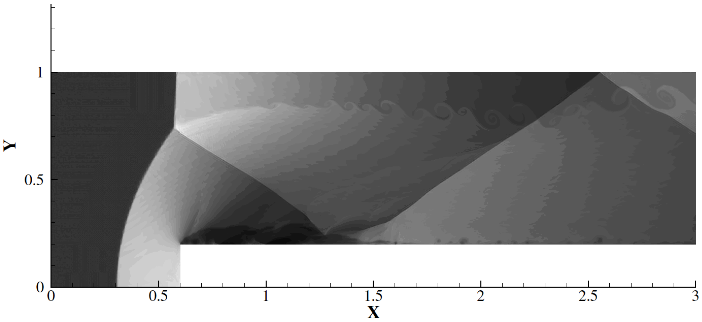

(d) DGP4, $h = 0.01$

FIGURE 8. Simulation results of the forward-facing-step case with different polynomial orders and mesh sizes.

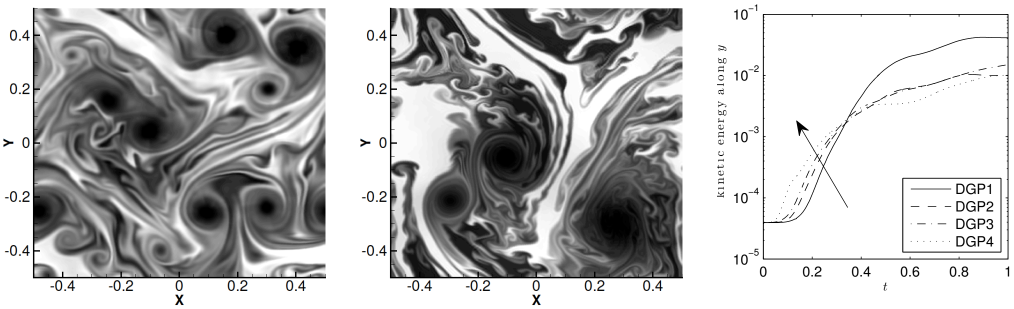

(a) DGP1 solution at $t = 5$ (b) DGP3 solution at $t = 5$ (c) Early growth of kinetic energy as a function of time

FIGURE 9. Simulation results of Kelvin-Helmholtz instability.

ity of discontinuities, which helps maximize the scheme's resolution for smooth solutions while localizing the shock-capturing errors.

In a future study, we will use this AV formulation for compressible turbulence simulations and extend DG's capability towards more complex flow physics.

## Acknowledgments

Financial support through the NSF CAREER program with award No. CBET-0844587 is gratefully acknowledged. Helpful discussions with Dr. Yee Chee See on stability analysis are greatly appreciated.

## REFERENCES

BARTER, G. & DARMOFAL, D. 2010 Shock capturing with PDE-based artificial viscosity for DGFEM: Part i. formulation. *J. Comp. Phys.* **229**, 1810–1827.

BASSI, F. & REPAY, S. 2000 *GMRES discontinuous Galerkin solution of the compressible Navier-Stokes equations.* In: Discontinuous Galerkin Methods: Theory, Computation and Applications, (ed. B. Cockburn & C. W. Shu), pp. 197–208. Springer.

CASONI, E., PERAIRE, J. & HUERTA, A. 2013 One-dimensional shock-capturing for high-order discontinuous Galerkin methods. *Int. J. Numer. Meth. Fluids* **71**, 737–755.

COCKBURN, B. & SHU, C. W. 1998 The Runge-Kutta discontinuous Galerkin method for conservation laws V: multidimensional systems. *J. Comp. Phys.* **141**, 199–224.

COCKBURN, B. & SHU, C.-W. 2001 Runge-Kutta discontinuous Galerkin methods for convection-dominated problems. *J. Sci. Comput.* **16** (3), 173–261.

GUERMOND, J.-L. & PASQUETTI, R. 2008 Entropy-based nonlinear viscosity for Fourier approximations of conservation laws. *C. R. Acad. Sci. Paris, Ser. I* **346**, 801–806.

HARTMANN, R. 2006 Adaptive discontinuous Galerkin methods with shock-capturing for the compressible Navier-Stokes equations. *Int. J. Numer. Meth. Fluids* **51**, 1131–1156.

KAWAI, S. & LELE, S. 2008 Localized artificial diffusivity scheme for discontinuity capturing on curvilinear meshes. *J. Comp. Phys.* **227**, 9498–9526.

KRIVODONOVA, L. 2007 Limiters for high-order discontinuous Galerkin methods. *J. Comp. Phys.* **226**, 879–896.

Lv, Y. & Ihme, M. 2013*a* Development of discontinuous Galerkin method for detonation and supersonic combustion. In *51st AIAA Aerospace Sciences Meeting including the New Horizons Forum and Aerospace Exposition*.

Lv, Y. & Ihme, M. 2013*b* Discontinuous Galerkin method for compressible viscous reacting flow. In *21st AIAA Computational Fluid Dynamics Conference*.

Lv, Y. & Ihme, M. 2014 Discontinuous Galerkin method for multicomponent chemically reacting flows and combustion. *J. Comp. Phys.* **270**, 105–137.

Nguyen, N., Persson, P.-O. & Peraire, J. 2007 RANS solutions using high order discontinuous Galerkin methods. AIAA 2007-914.

Persson, P.-O. & Peraire, J. 2006 Sub-cell shock capturing for discontinuous Galerkin methods. AIAA 2006-112.

Qiu, J. & Shu, C.-W. 2005 Hermite WENO schemes and their application as limiters for Runge-Kutta discontinuous Galerkin method II: two dimensional case. *Comput. Fluids* **34**, 642–663.

Rusanov, V. 1961 Calculation of intersection of non-steady shock waves with obstacles. *J. Comput. Math. Phys. USSR* **1**, 267279.

Woodward, P. & Colella, P. 1984 The numerical simulation of two-dimensional fluid flow with strong shocks. *J. Comp. Phys.* **54**, 115–173.

Yu, J. & Yan, C. 2013 An artificial diffusivity discontinuous Galerkin scheme for discontinuous flows. *Comput. & Fluids* **75**, 56–71.

Zingan, V., Guermond, J.-L., Morel, J. & Popov, B. 2013 Implementation of the entropy viscosity method with the discontinuous Galerkin method. *Comput. Method Appl. M.* **253**, 479–490.